JOURNAL OF NANO- AND ELECTRONIC PHYSICS
Vol. **18** No 5, 05014(9pp) (2026)

ЖУРНАЛ НАНО- ТА ЕЛЕКТРОННОЇ ФІЗИКИ
Том **18** № 5, 05014(9cc) (2026)

OPEN ACCESS

REGULAR ARTICLE

Synthesis and Characterization of $CuCr_{1.4}Co_{0.6}O_4$ Spinel Nanostructures: Impact of Cobalt Doping on Optical and Photocatalytic Properties

Soumaia Khaldi[1,*], Abdelfattah Allaoui[1], Louiza Zenkhri[1], Safa Besra[2], Ece T. Saka[3], Cagla Akkol[3]

[1] *Laboratory for Valorization and Promotion of Saharian Ressources (VPRS), Chemistry Department, Kasdi Merbah University, UKMO, 30000 Ouargla, Algeria*
[2] *Laboratory for Development of New and Renewable Energies in Arid and Saharan Zones (LENREZA), Physical Department, Kasdi Merbah University, UKMO, 30000 Ouargla, Algeria*
[3] *Inorganic Research Laboratories, Chemistry Department, Karadeniz Technical University, KTU, 61080 Trabzon, Turkiye*

(Received 08 April 2026; revised manuscript received 24 October 2026; published online 28 October 2026)

In this work, copper-based spinel oxides with the general formula $CuCr_{2-x}Co_xO_4$ ($x = 0$ and 0.6) were synthesized via a facile combustion method to investigate the effect of cobalt incorporation on their structural, morphological, optical, and photocatalytic properties. The samples were characterized using X-ray diffraction (XRD), scanning electron microscopy coupled with energy-dispersive spectroscopy (SEM–EDS), and UV–visible diffuse reflectance spectroscopy (UV–DRS). XRD confirmed the formation of well-crystallized single-phase spinel structures for both $CuCr_2O_4$ and $CuCr_{1.4}Co_{0.6}O_4$, with nanoscale crystallite sizes, indicating that cobalt substitution preserved the spinel framework. SEM images revealed agglomerated nanosized grains with nearly spherical morphology, while EDS confirmed the homogeneous distribution of Cu, Cr, O, and Co. UV–DRS analysis showed a decrease in the optical band gap from 2.81 eV ($CuCr_2O_4$) to 2.65 eV ($CuCr_{1.4}Co_{0.6}O_4$), suggesting enhanced light absorption. The photocatalytic performance of the samples was evaluated under UV irradiation toward the degradation of methylene blue (MB) and 4-nitrophenol (4-NP). The doped $CuCr_{1.4}Co_{0.6}O_4$ exhibited markedly superior photocatalytic activity, achieving complete MB degradation and 72.9 % conversion of 4-NP within 15 min, outperforming the undoped $CuCr_2O_4$.This enhancement is attributed to improved charge separation efficiency, reduced band gap energy, and smaller crystallite size resulting from cobalt incorporation.

Keywords: Spinel nanostructures, Combustion method, Optical properties, Photocatalysis, 4-nitrophenol.

DOI: 10.21272/jnep.18(5).05014 PACS numbers: 81.20.Ka, 81.07.Bc, 82.50.Hp.

1. INTRODUCTION

Semiconductor nanomaterials have become increasingly pivotal in modern research due to their highly tenable physicochemical properties and significant potential to address global challenges in energy harvesting, environmental remediation, and nanoelectronics technologies [1-3].

Within this broad class of materials, metal oxide synthesized at the nanoscale are particularly attractive. They provide enhanced structural homogeneity, improved mass transport, and superior thermal and chemical stability, making them strong candidates for applications that require robustness and controlled physicochemical performance [4]. Among these, spinel oxides with the general formula AB_2O_4 have garnered substantial interest because of their structural flexibility and rich electronic behavior. The spinel lattice can host a variety of cations in both tetrahedral (A) and octahedral (B) sites, which allows deliberate modulation of the band structure, conductivity, redox behavior, oxygen-vacancy concentration, and even magnetic properties via cation substitution [5]. The structural tunability and compositional flexibility of spinel oxides render them highly versatile functional materials, enabling their deployment in diverse technological fields such as heterogeneous catalysis, gas sensing, lithium-ion battery electrodes, ceramic pigments, electronic devices, and photocatalysis [5-10]. Within this class of materials, copper chromite ($CuCr_2O_4$) has emerged as a particularly promising candidate. As a p-type semiconductor, $CuCr_2O_4$ exhibits strong absorption in the visible-light region, notable chemical and thermal robustness, and distinctive catalytic and magnetic properties [11-14]. Owing to these attributes, $CuCr_2O_4$ has been extensively investigated for applications in catalytic combustion, electrochemical processes, and the degradation of organic pollutants [15, 16]. However, the photocatalytic efficiency of $CuCr_2O_4$ is often limited by intrinsic factors such as modest surface area, rapid recombination of photogenerated charge carriers, and limited light absorption [11, 12]. To overcome these limitations, substitution of Cr^{3+} with transition-metal ions, particularly Co, has been widely explored to modify the crystal field, introduce mid-gap states, adjust M-O-M bonding, and improve charge separation and optical absorption [10, 11]. Cobalt incorporation into the spinel framework is expected to induce local lattice distortions, modify the electronic configuration, and strengthen p-d orbital interactions, potentially enhancing both optical

* Correspondence e-mail: khaldi.soumaia@univ-ouargla.dz

© 2026 The Author(s). Journal of Nano- and Electronic Physics published by Sumy State University. This article is distributed under the terms and conditions of the Creative Commons Attribution (CC BY) license.

Cite this article as: S. Khaldi, et al., *J. Nano- Electron. Phys.* 18 No 5, 05014 (2026) https://doi.org/10.21272/jnep.18(5).05014

absorption and photocatalytic reactivity.

Various methods exist to prepare $CuCr_2O_4$ nanomaterials, including hydrothermal synthesis, co-precipitation, and combustion methods [17-19]. In this study, we employed a facile combustion method, which is rapid, cost-effective, and efficient in producing spinel nanomaterials with high crystallinity and controlled morphology.

In this study, pure $CuCr_2O_4$ and cobalt-modified copper chromite ($CuCr_{1.4}Co_{0.6}O_4$) were synthesized via a solution-combustion method. Their structural, morphological, and optical properties were characterized using XRD, SEM/EDS, and UV-DRS, and their photocatalytic performance was evaluated through the degradation of methylene blue (MB) and the oxidation of 4-nitrophenol (4-NP) under UV irradiation. Cobalt incorporation into the $CuCr_2O_4$ lattice induced structural and electronic modifications that enhanced light absorption and charge separation, resulting in a significantly improved photocatalytic activity. To the best of our knowledge, this work is the first to investigate cobalt substitution specifically at the B site of the $CuCr_2O_4$ spinel lattice, formulated as$CuCr_{1.4}Co_{0.6}O_4$ via combustion synthesis, and to directly correlate this targeted modification with the resulting structural, optical, and photocatalytic behavior.

2. EXPERIMENTAL

2.1 Materials

All chemicals were of analytical grade and were used without any additional purification. Copper nitrate hexahydrate ($Cu(NO_3)_{2.6}H_2O$, Merck, Germany), chromium nitrate nonahydrate ($Cr(NO_3)_{3.9}H_2O$, RECTAPUR PROLABO), and cobalt nitrate hexahydrate ($Co(NO_3)_{2.6}H_2O$, Biochem Chemopharma) served as the sources of metal ions. Urea (H_2NCONH_2) from RECTAPUR PROLABO acted as a fuel during the combustion process. Methylene blue from IBI scientific, 4-Nitrophenol from Sigma – Aldrich (USA), and hydrogen peroxide (H_2O_2, 30 % wt.) from MERCK (Germany) utilized to perform the photocatalytic experiment. All aqueous solutions were freshly prepared using bidistilled water.

2.2 Samples Synthesis

Copper chromite pure (CSP) and cobalt-doped copper chromite (CSCo) spinel oxides were synthesized by a facile combustion method. Precisely measured amounts of copper nitrate (10 mmol), chromium nitrate (20 mmol), and urea (30 mmol) were dissolved in 60 mL of bidistilled water and magnetically stirred at 90 °C until a homogeneous solution was obtained.

For the doped sample (CSCo), part of the chromium precursor was substituted with cobalt nitrate to achieve the nominal composition $CuCr_{1.4}Co_{0.6}O_4$, while maintaining the same total metal content as the undoped sample. The same synthesis procedure was applied to both compositions to ensure comparable conditions.

The resulting solution was slowly heated to about 100 °C to form a viscous gel, followed by further heating to approximately 250 °C, till the combustion reaction happened and produced a fluffy, ash-like powder. The obtained materials were gently ground in an agate mortar and then calcined at 600 °C for 3 h to yield crystallization and formation of the spinel phase.

2.3 Samples Characterization

The crystal structures of the prepared spinel oxides (CSP and CSCo) were analyzed using a PANalytical X'Pert^3 Powder X-ray diffractometer equipped with Cu Kα radiation ($\lambda = 1.5406$ Å). Diffraction patterns were collected over a 2θ range of 5° to 80° with a scan step of 0.026°. The structural data were refined using HighScore Plus software (PANalytical) based on reference data from the Crystallographic Open Database (COD). The surface morphology and particle distribution were examined using a scanning electron microscope (SEM, Zeiss EVO LS10) equipped with an EDAX Element-C2B X-ray detector. The elemental composition and distribution were confirmed using energy-dispersive X-ray spectroscopy (EDS) and mapping analysis using the Smart CPS Mapping system (EDAX Inc., 2019, AMETEK Inc.), which verified the uniform presence of copper, chromium, cobalt, and oxygen in the synthesized samples. The optical absorption properties were studied using a Specord 200 Plus UV-Vis spectrometer operating in the diffuse reflectance (UV-DRS) mode. The optical band gap energy (E_g) for each sample was estimated from the diffuse reflectance data using the Kubelka-Munk function.

2.4 Photocatalytic Tests

The photocatalytic efficiency of the prepared copper spinel chromate (CSP) and cobalt substituted copper chromite (CSCo) oxides was investigated by decomposing methylene blue (MB) and oxidizing 4-nitrophenol (4-NP) under ultraviolet irradiation. All reactions were carried out in a stirred photoreactor equipped with thirteen UV lamps, operating at room temperature.

For the MB assay, 50 mL of aqueous MB solution (2×10^{-5} mol·L^{-1}) was mixed with 30 mg of the photocatalyst. The suspension was magnetically stirred in the dark for approximately 30 minutes to reach adsorption-desorption equilibrium. Irradiation was then initiated while stirring continuously. At specific time intervals (3, 10, 20, 40, 60, and 80 minutes), 2 mL of the suspension was withdrawn, filtered, and analyzed. In another set of experiments, 50 µL of hydrogen peroxide (30 %) was added after three minutes of illumination to evaluate an additional oxidizing effect. MB concentration changes were monitored using a Perkin-Elmer Lambda 25 UV-Vis spectrometer at 664 nm using a 1 cm quartz cuvette. Decomposition yield was assessed using:

$$\text{Degradation\% (D\%)} = \left(\frac{C_0 - C_t}{C_0}\right) \times 100 \qquad (1)$$

C_t at time (t_{min}) and C_0 at initial time or time zero (0min) are the concentration of MB solution.

The photooxidation of 4-nitrophenol (4-NP) under ultraviolet illumination was employed to evaluate the photocatalytic behavior of the obtained copper chromite materials (CSP and CSCo). The procedure was carried out in accordance with the approach reported by Ece T. S. et al. [20]. Controlled amounts of the reactant, catalyst, and oxidizing agent were introduced into a Schlenk

flask and subjected to UV exposure for 15 minutes. During the reaction, aliquots were withdrawn at defined times (0, 5, 10, and 15 min), and the progress of 4-NP conversion (%) was analyzed by gas chromatography (GC) to determine the overall reaction efficiency.

3. RESULTS AND DISCUSSION

3.1 XRD Study

The XRD patterns of the synthesized $CuCr_2O_4$ (CSP) and Co-doped $CuCr_2O_4$ (CSCo) spinel oxides prepared by the combustion method are shown in Fig. 1. The diffraction peaks of the undoped sample (CSP) which located at $2\theta = 18.53°$, 29.58°, 31.12°, 35.28°, 37.72°, 42.30°, 46.59°, 53.43°, 56.34°, 57.95°, 61.58°, 64.87°, 74.45°, and 80.61°, respectively. They are well matched with the (101), (200), (112), (211), (202), (220), (301), (312), (321), (303), (400), (411), (422),and (404) lattices planes of tetragonal of $CuCr_2O_4$ spinel phase with the standard JCPDS card (no. 00-034-0424), confirming the formation of a pure spinel oxide without secondary impurities [21].

After cobalt doping, the main $CuCr_2O_4$ spinel reflections remain present, indicating that the spinel structure is largely retained. A slight shift of the diffraction peaks toward higher 2θ values are observed, suggesting a minor lattice contraction resulting from the substitutional incorporation of Co^{2+} ions into the $CuCr_2O_4$ lattice.

Additionally, very weak peaks around $2\theta = 36.40°$, and 44.00° (indexed by *) correspond to Co_3O_4 with the standard JCPDS card (no. 01-080-1540), and a faint feature at $2\theta = 49.00°$ (indexed ■) can be assigned to CuO with the standard JCPDS card (no. 00-041-0254), implying the presence of trace amounts of cobalt and copper oxides. These observations confirm that cobalt is mainly incorporated into the $CuCr_2O_4$ spinel structure, which previously observed also in this literature [22] with only limited segregation of secondary phases.

The sharp and intense diffraction peaks for both samples confirm their high degree of crystallinity. For all materials, the (211) reflection exhibits the highest intensity, further verifying the formation of a well-developed $CuCr_2O_4$ spinel structure, in accordance with earlier studies [21, 23].

The average crystallite size (D) of the samples was calculated using the Scherrer's empirical Eq. 2:

$$D = \frac{k\lambda}{\beta cos\theta} \quad (2)$$

Where k, λ, β and θ are the Scherrer constant (from 0.62 to 2.08 and is usually taken as about 0.9), the wavelength of X-ray source ($\lambda_{Cu} = 0.15418$), FWHM: Full-Width at Half- Maximum of the XRD patterns peak, and Bragg diffraction angle, respectively [24, 25].

The crystallite sizes were calculated to be 65 nm for CSP and 49 nm for CSCo. The reduction in crystallite size upon Co substitution is attributed to the replacement of Cr^{3+} ions (0.615 Å) by the slightly smaller Co^{3+} ions (0.545 Å), generating local lattice strain that suppresses crystallite growth during combustion synthesis. Similar ionic-radius-driven crystallite size variations in doped spinels have been reported by Xu et al. [26]. The nanoscale crystallinity of both samples confirms that the combustion method is highly effective in producing well-crystallized spinel oxides suitable for photocatalytic applications.

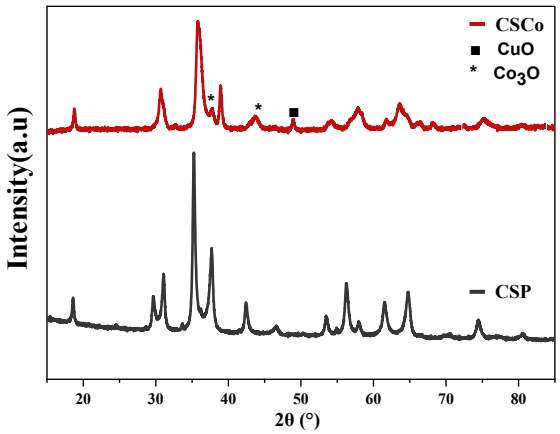


Fig. 1 – The XRD pattern of synthesized materials

3.2 Morphological and Elemental Composition by SEM/EDS

The surface morphology of the synthesized copper chromite (CSP) and Co-doped copper chromite (CSCo) spinel oxides was examined by SEM at magnifications of 10 μm and 1 μm, as shown in Fig. 2 (a and b). Both samples exhibit agglomerated microstructures composed of irregular nanoscale grains, which is typical for combustion derived spinels due to the rapid gas evolution and highly exothermic reaction that promote fast nucleation and particle clustering.

The SEM micrographs of the undoped $CuCr_2O_4$ (CSP) sample (Fig. a_1-a_2) reveal a relatively compact surface composed of strongly aggregated particles. The particle size distribution (Fig. a_3) indicates an average grain size of 115 nm, reflecting significant agglomeration. Similar compact nanoparticulate morphologies have been reported for $CuCr_2O_4$ synthesized via solution combustion ,where nanoscale grains fuse into clusters due to high local temperatures and rapid combustion kinetics [27].

In contrast, the Co-doped $CuCr_{1.4}Co_{0.6}O_4$ (CSCo) sample (Fig. b_1-b_2) exhibits a noticeably different morphology, characterized by smaller grains, more uniform dispersion, and a rougher, more fragmented surface. The corresponding histogram (Fig. b_3) confirms a reduction in mean particle size (95 nm), indicating that cobalt incorporation effectively suppresses grain growth during combustion. This behaviour is consistent with previous reports showing that B site cation substitution modifies diffusion pathways and crystallization dynamics, thereby limiting particle coarsening in combustion synthesized spinels [28].

The reduced grain size and increased surface roughness in the doped CSCo sample are expected to enhance photocatalytic performance by improving light absorption, increasing the density of active surface sites, and facilitating more efficient charge carrier transport.

These morphology-induced enhancements align with the crystallite-size reduction observed in XRD results, noting that the larger apparent SEM particle size arises from agglomerates composed of multiple crystallites.

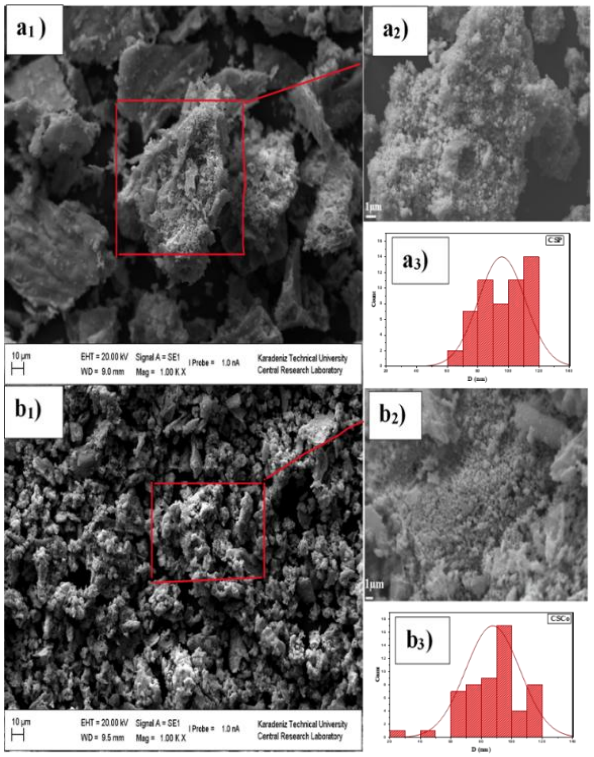


Fig. 2 – SEM images and grain size distribution of: CSP (a), CSCo (b) EDX patterns of CSP (on the left), and CSCo (on the right)

To complement the SEM observations, EDS analysis (Fig. 3) was performed to confirm the elemental composition and the success of cobalt substitution. For the undoped $CuCr_2O_4$ (CSP) sample, only Cu, Cr, and O were detected, and their quantitative ratios (O = 24.92 wt%, Cr = 46.41 wt%, Cu = 28.68 wt%) closely align with the theoretical stoichiometry, indicating the formation of a chemically pure single-phase spinel. In contrast, the Co-doped $CuCr_{1.4}Co_{0.6}O_4$ (CSCo) sample exhibits additional Co peaks alongside Cu, Cr, and O, with a cobalt content of 15.48 wt% (9.67 at%), which corresponds well with the targeted substitution level ($x = 0.6$). The partial decrease in chromium proportion further confirms cationic replacement at the B-site. Moreover, elemental mapping (Fig. 4) demonstrates a uniform spatial distribution of Cu, Cr, Co, and O without evidence of secondary phases or Co rich clusters, signifying that the combustion process ensured homogeneous mixing of the metal precursors and effective incorporation of cobalt into the spinel lattice. These findings validate the successful synthesis of compositionally and structurally uniform CSP and CSCo spinel oxides.

3.3 Optical Properties and Band Gap

The optical behavior of the synthesized $CuCr_2O_4$ (CSP) and Co-doped $CuCr_2O_4$ (CSCo) spinel oxides was assessed using UV–Vis diffuse reflectance spectroscopy (DRS), as illustrated in Fig. 5 (a–b). The diffuse reflectance spectra (Fig. 5a) show a clear difference between the two samples. The undoped $CuCr_2O_4$ (CSP) exhibits relatively high and nearly constant reflectance throughout the visible region (400-700 nm), followed by a gradual increase toward the near-infrared (NIR) region.

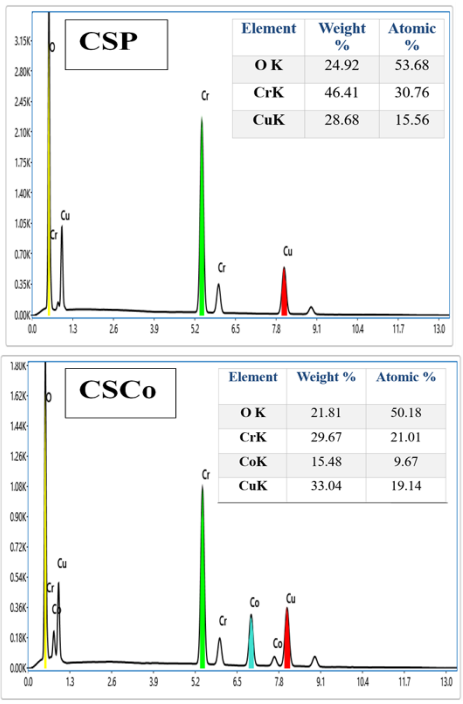


Fig. 3 – EDX patterns of CSP, and CSCo

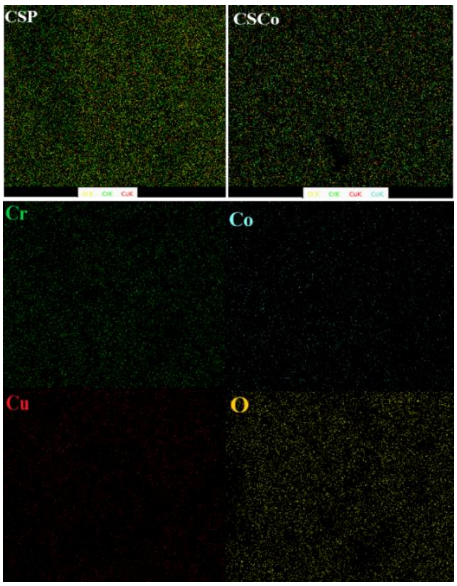


Fig. 4 – Elemental mapping of Cr, Co, Cu, and O in CSP and CSCo

This spectral behavior is characteristic of semiconducting spinel oxides and confirms the non-metallic nature of $CuCr_2O_4$ in agreement with earlier reports [29, 30]. In the visible range, the optical absorption of $CuCr_2O_4$ arises mainly from d-d electronic transitions of Cu^{2+} ($3d^9$) and Cr^{3+} ($3d^3$) ions and from $O^{2-} \rightarrow Cr^{3+}$ charge-transfer transitions [29, 31].

Upon cobalt incorporation, the CSCo sample displays a significant reduction in reflectance across both the visible and NIR regions, indicating enhanced photon absorption. This modification is consistent with a narrowing of the band gap, attributed to the partial substitution of Cr^{3+} by Co^{2+}/Co^{3+} ions, which introduces additional Co $3d$ states near the conduction band and strengthens O $2p$ – Co $3d$ hybridization [30, 32]. Such

electronic restructuring promotes improved visible-light harvesting and modifies the electronic transitions within the spinel lattice.

The band gap energies were estimated using the Kubelka–Munk function, assuming direct allowed transitions, according to the relation [6, 33]:

$$(\mathrm{F(R)} * h\nu)^2 = A.(h\nu - E_{bg}) \quad (3)$$

Here, A is a constant, $h\nu$ represent the photon's energy, F indicates a function of the Kubelka-Munk model, and R represents its reflection published in the Kubelka-Munk function [33]. The F function can be calculated using Eq. 4:

$$F = \frac{K}{S} = \frac{(1-R)^2}{2R} \quad (4)$$

Where R, S and K are the reflectance, the scattering coefficient and the absorption coefficient, respectively.

Fig. 5 (b) shows the plot of $(\mathrm{F(R)} * h\nu)^2$ versus $h\nu$ for both (CSP) and (CSCo). The band gap values were determined by extrapolating the linear portion of the plot to the photon energy axis, yielding $E_g = 2.81$ eV for CSP and 2.65 eV for CSCo. The decrease in band gap after cobalt substitution confirms enhanced visible light absorption and suggests improved charge carrier mobility and electronic delocalization within the Co-modified spinel lattice [32, 34]. This band-gap narrowing is particularly advantageous for photocatalytic and opted applications.

3.4 Photocatalytic Test

3.4.1 Photodegradation of MB

Fig. 6 (a–d) displays the UV–Vis absorbance spectra of MB solutions irradiated in the presence of CSP and CSCo, with and without the addition of H_2O_2. A progressive reduction in absorbance intensity was observed with increasing irradiation time, indicating the continuous degradation of MB. Notably, the CSCo sample exhibited a considerably faster decrease in absorbance compared to CSP, demonstrating its superior photocatalytic activity.

The photodegradation efficiency (D%) and the temporal concentration decay (C_t/C_0) for all samples are presented in Fig. 7 (a and c). After 80 min of UV irradiation, CSP and CSCo achieved degradation efficiencies of 71.29 % and 96.61 %, respectively, in the absence of H_2O_2. Upon addition of H_2O_2, the efficiencies increased to 89.99 % for CSP and nearly complete degradation for CSCo. The enhancement induced by H_2O_2 is attributed to the generation of additional reactive oxygen species (ROS), primarily hydroxyl radicals (•OH), which accelerate the oxidation of MB.

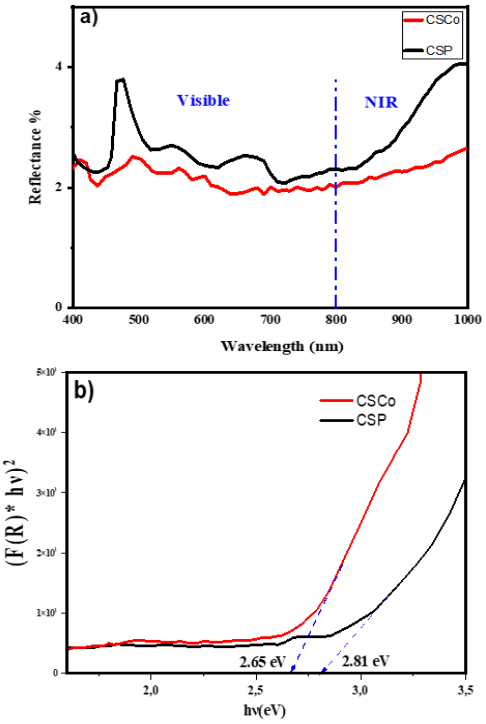


Fig. 5 – Reflectance spectra of CSP and CSCo (a), Plot of $(\mathrm{F(R)} * h\nu)^2$ versus $h\nu$ for the samples (b)

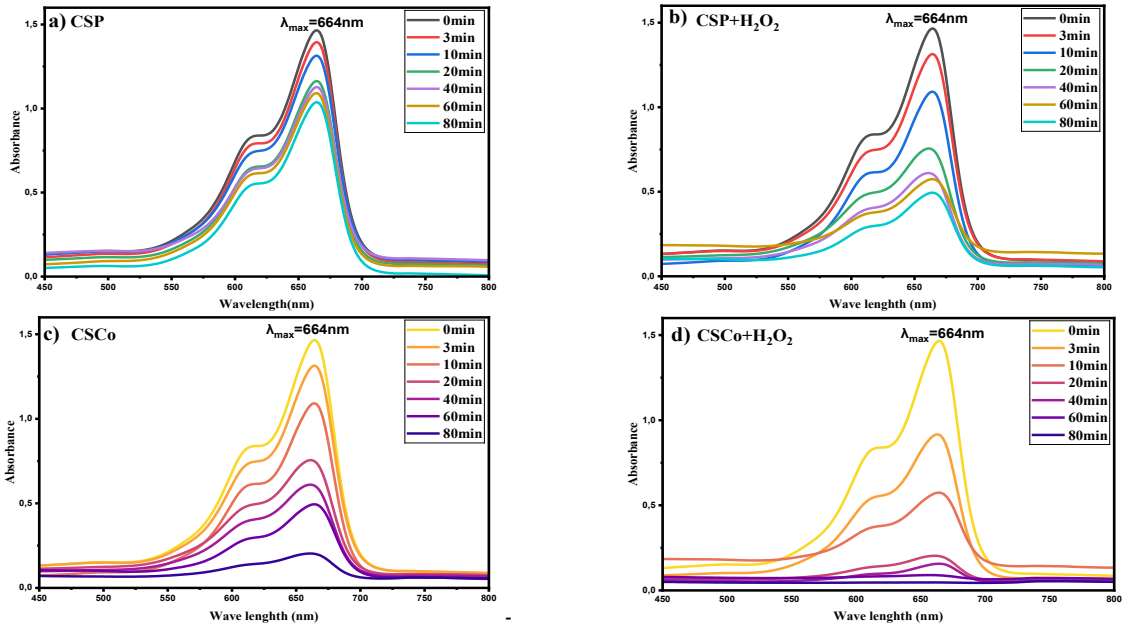


Fig. 6 – UV-Vis spectra of MB photodegradation by synthesized spinel oxides: CSP (a), CSP+ H_2O_2 (b), CSCo (c), CSCo+H_2O_2 (d)

Table 1 – The rate constant k_{app}(min^{-1}) and correlation coefficients R^2 for MB degradation under 80 min of irradiation time

Photocatalyst	**CSP**	**CSP+ H_2O_2**	**CSCo**	**CSCo+ H_2O**
k_{app} (min^{-1})	0.00405	0.01649	0.01940	0.04298
R^2	0.85309	0.93438	0.95897	0.97503

The superior photocatalytic performance of the Co doped $CuCr_2O_4$ (CSCo) can be attributed to its physico-chemical characteristics as confirmed by UV-Vis (DRS), SEM, and XRD analyses. Firstly, CSCo exhibited a narrower optical band gap energy (2.65 eV) than the undoped CSP (2.81 eV), which facilitates more efficient photoexcitation under UV irradiation. Moreover, the doped sample displayed a smaller average particle size (95 nm) compared to CSP (105 nm), providing a large surface area and more active sites for photocatalytic reactions.

To understand the photodegradation kinetics of the samples, the data have been adjusted to zero, the first and second model as following [6]:

$$C_0 - C_t = k_{app} \cdot t \quad (5)$$

$$\ln \frac{C_0}{C_t} = k_{app} \cdot t \quad (6)$$

$$\left(\frac{1}{C_t}\right) - \left(\frac{1}{C_0}\right) = k_{app} \cdot t \quad (7)$$

Where C_t, C_0, and k_{app} are the concentration of MB at time t and $t = 0$, and the rate constant, respectively.

Fig. 7 c shows the Plots of ln (C_0/C_t) vs irradiation time for all samples, both with and without H_2O_2. The high linearity and correlation coefficient (R^2) confirm that the photodegradation of MB follows a pseudo first order kinetic model. The rate constants (k_{app}) were obtained from the slopes of these plots and correlation coefficients R^2 summarized in Table 1.

It is evident that the photocatalytic degradation rate of CSCo was 4.79 times higher than that of CSP, while the degradation rate of CSCo + H_2O_2 was 2.61 time of CSP + H_2O_2.These results confirm the positive impact of Cobalt doping and H_2O_2 addition on the photocatalytic efficiency of $CuCr_2O_4$ spinel oxides.

Fig. 7 b shows the possible schema mechanism of the MB photodegradation by doped copper chromite spinel oxide $CuCr_{1.4}Co_{0.6}O_4$ (CSCo). Firstly, under UV-irradiation, electron in the spinel oxide are excited from VB to CB, leading to the creation of electrons-holes pairs, where (e^-) in (CB) and (h^+) in (VB).

$$CuCr_{1.4}Co_{0.4}O_4 + h\nu \rightarrow e^-(\mathrm{CB}) + h^+(VB) \quad (8)$$

Subsequently, the electrons (e^-) in (CB) captured by dissolved O_2 in water or absorbed O_2 on the surface of photocatalyst to form superoxide ion radicals ($O_2^{\bullet -}$); the holes reacted with water molecules (H_2O) to generate hydroxyl radicals ($OH^\bullet$) [6, 35].

$$e^-(\mathrm{CB}) + O_2 \rightarrow O_2^{\bullet -} + h^+(VB) \quad (9)$$

$$h^+(VB) + H_2O \rightarrow OH^\bullet + H^+ \quad (10)$$

In the present study, we have added hydrogen peroxide (H_2O_2) to the photocatalyst $CuCr_{1.4}Co_{0.6}O_4$.H_2O_2 plays as generator of free radicals by interacting with excited electrons of photocatalyst. Therefore, the added of H_2O_2 helps to improve the degradation rate of the photocatalyst by producing extra radicals ($OH^\bullet$) for facilitating photocatalytic activity, which is consistent with previous reports [6, 35].

$$e^-(\mathrm{CB}) + H_2O_2 \rightarrow OH^\bullet + OH^- \quad (11)$$

Finally, the reactive species formed, which are strong oxidants ($OH^\bullet$) and ($O_2^{\bullet -}$), can decompose organic dyes (MB) into carbon dioxide, water moieties and other degraded products [6].

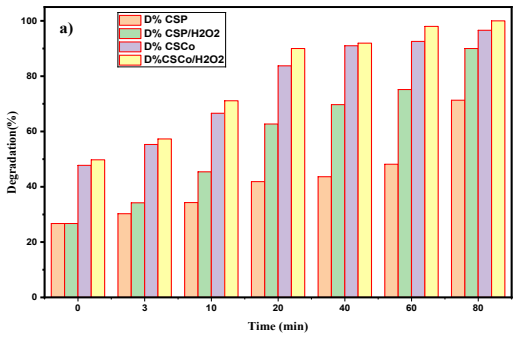
$$MB + OH^\bullet \rightarrow MB^{\bullet +} + OH^- \quad (12)$$

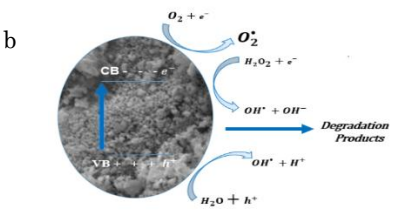
$$MB^{\bullet +} + O_2^{\bullet -} \rightarrow CO_2 + H_2O + degraded\ products \quad (13)$$

3.4.2 Photooxidation of 4-NP

Numerous intermediates have been reported in the photocatalytic degradation mechanism of 4-nitrophenole (4-NP) via advanced oxidation processes (AOPs), including 4-nitrocatechol, hydroquinone, 1,2,4-trihydroxybenzen and benzoquinone [20, 36-38]. In the present work, GC analysis confirms the formation of hydroquinone (HQ) and benzoquinone (BQ). Similar results have been reported elsewhere [20, 38]. Table 2 presents the turnover number (TON), turnover frequency (TOF), conversion (%) and selectivity (%) of the oxidation products during the photocatalytic oxidation of 4-NP using CSP and CSCo. The findings demonstrated that both photocatalysts promoted the oxidation of 4-NP under UV irradiation, yielding benzoquinone (BQ) and hydroquinone (HQ) as the main reaction products.

As shown in Fig. 8 a, the total conversion of 4-NP using the synthesized spinel. It was noted that the highest conversion was achieved with doped copper chromite (CSCo), reaching 72.9 %, while for pure copper chromite (CSP), it reached 52.7 %. Moreover, Fig. 8 b. demonstrates that CSCo maintained a 26.11 % conversion even after five cycles, confirming its strong reusability and stability.





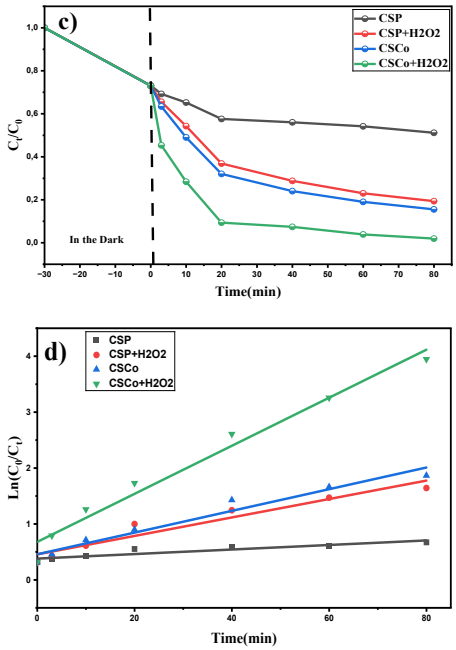


Fig. 7 – Degradation efficiency of MB on photocatalyst without H_2O_2 and with add H_2O_2 (a), Schematic of the proposed mechanism of MB photodegradation using CSCo (b), Time dependent photocatalytic degradation of MB on photocatalyst without and with add H_2O_2 curves (c), Graphs of $\ln(C_0/C_t)$ vs irradiation time for all samples without and with add of H_2O_2 (d)

These observations align with the improved physicochemical features of the doped spinel. Such as enhanced charge separation, reduced recombination, and optimized band gap energy, as confirmed by XRD, UV, and SEM analyses.

The overall mechanism of 4-NP photooxidation by the synthesized spinel photocatalyst under UV light can be summarize on four steps; the two primary steps are presented in Fig.7.b; which are the excitation of spinel oxides and the formation of reactive species ($O_2^{\cdot-}$ and $OH^{\cdot}$) from Eqs. (8) to (10). The third step was the degradation of 4-NP by hydroxyl radicals and superoxide anions ($OH^{\cdot}$ and $O_2^{\cdot-}$).The attack of reactive species on 4-NP molecules, the nitro group NO_2 undergoes reduction, and the aromatic ring undergoes hydroxylation at the para positions, which leads to the formation of HQ and BQ as primary and secondary products, respectively [20, 38]. The fourth step is the further oxidation of the primary products; hydroquinone may oxidize to benzoquinone and complete mineralization to carbon dioxide and water.

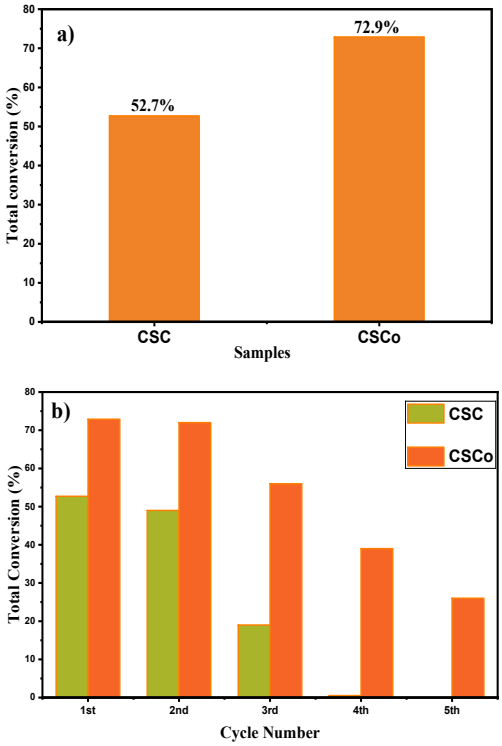


Fig. 8 – Percentage total conversion (%) of 4-NP during time reaction by CSP and CSCo (a), recycling experiments of 4-NP using the samples (b)

Table 2 – Selective photooxidation of 4-NP with all samples (CSP, and CSCo)

Photocatalyst	Conversion (%)		Selectivity (%)		TON	TOF (h^-)
	BQ	HQ	BQ	HQ		
CSP	22.7	30.3	43.07	57.49	263,5	1054
CSCo	27.7	42.9	37.9	58.8	364,5	1458
All photocatalytic reaction were done with the same condition in photoreactor with UV light during 15 min at $T = 25$ °C and ratio (1/300/500) Catalyst/Oxidant/Substrate (4-NP). Masse of catalyst = 2 mg; mole of 4-NP = mole of catalyst × 500; mole of oxidant = mole of catalyst × 300 TON = mole of product/mole of catalyst. TOF = mole of product/mole of catalyst × time.						

4. CONCLUSION

In this study, pure and cobalt doped copper chromite spinel oxides with formula $CuCr_{2-x}Co_xO_4$ ($x = 0$ and 0.6) were successfully synthesized via a facile combustion method and evaluated as photocatalysts for the degradation of organic pollutants (MB, and 4-NP). XRD analyses confirmed the formation of spinel phase for both samples, with average crystallite sizes of 65 nm for CSP and 49 nm for CSCo, indicating that cobalt substitution effectively crystal growth. SEM analysis ag-glomerated, nanosized grains with average size of 115 nm (CSP) and 95 nm (CSCo). UV Vis DRS analysis showed that Co doping reduced the optical band gap from 2.81 eV to 2.65 eV, enhancing light absorption and electron–hole generation. Photocatalytic tests demonstrated that CSCo exhibited superior activity toward both methylene blue (MB) degradation and 4-nitrophenol (4-NP) oxidation under UV irradiation, achieving a total degradation of MB and 72.9 % conversion of 4-NP within 15 min, along with excellent reusability after multiple cycles. The improvement in photocatalytic efficiency is attributed to the combined effects of smaller crystallite size, reduced band gap, and enhanced charge separation induced by cobalt doping. These findings highlight Co doped $CuCr_2O_4$ as a promising and stable photocatalyst for the efficient removal of organic pollutants from aqueous media.

REFERENCES

1. N. Hossain, M.H. Mobarak, M.A. Mimona, M.A. Islam, A. Hossain, F.T. Zohura, M.A. Chowdhury, *Res. Eng.* **19**, 101347 (2023) https://doi.org/10.1016/j.rineng.2023.101347.
2. F. Zhang, X. Wang, H. Liu, C. Liu, Y. Wan, Y. Long, Z. Cai, *Appl. Sci.* **9** No 12, 2489 (2019) https://doi.org/10.3390/app9122489.
3. J. Fang, Z. Zhou, M. Xiao, Z. Lou, Z. Wei, G. Shen, *InfoMat* **2** No 2, 291 (2020) https://doi.org/10.1002/inf2.12067.
4. N. Joshi, D.K. Pandey, B.G. Mistry, D.K. Singh, *Nanomaterials: Advances and Applications,* 103 (Singapore: Springer Nature Singapore: 2023). https://doi.org/10.1007/978-981-19-7963-7_5.
5. D. Srikala, S.D. Kaushik, M. Verma, *Phys. Solid State* **66** No 9, 327 (2024) https://doi.org/10.1134/S1063783424601073.
6. S. Khaldi, A. Allaoui, L. Zenkhri, S. Besra, E.T. Saka, C. Akkol, H. Belkhalfa, *Solid State Commun.* **409**, 116307 (2026) https://doi.org/10.1016/j.ssc.2025.116307.
7. Z. Hu, X. Tang, X. Ma, S.Q. Guo, M. Zhen, J. Ning, B. Shen, *Chemosphere* **352**, 141428 (2024) https://doi.org/10.1016/j.chemosphere.2024.141428.
8. Y. Li, Z. Yuan, F. Meng, *Sensors* **20** No 18, 5413 (2020) https://doi.org/10.3390/s20185413.
9. Y. Gong, W. Ding, Z. Li, R. Su, X. Zhang, J. Wang, C. Sun, *ACS Catalysis* **8** No 5, 4082 (2018) https://doi.org/10.1021/acscatal.7b04401.
10. R. Bagtache, K. Boudjedien, I. Sebai, D. Meziani, M. Trari, *Appl. Phys. A* **127** No 1, 60 (2021) https://doi.org/10.1007/s00339-020-04198-7.
11. K. Patel, M. Patil, Y. Abhale, K.Y.A. Lin, K.B. Tan, A. Chauhan, S. Ghotekar, *Nanoscale* (2025) https://doi.org/10.1039/D5NR03084F.
12. M.B. Shafqat, M. Ali, S. Atiq, S.M. Ramay, H.M. Shaikh, S. Naseem, *J. Mater. Sci.: Mater. Electron.* **30** No 19, 17623 (2019) https://doi.org/10.1007/s10854-019-02111-4.
13. R. Shafique, M. Rani, A. Mahmood, S. Khan, N.K. Janjua, M. Sattar, T. Yaqoob, *Int. J. Environ. Sci. Technol.* **19** No 8, 7517 (2022) https://doi.org/10.1007/s13762-021-03616-4.
14. S. Balasurya, A.M. Elgorban, A.H. Bahkali, M.T. Yassin, R. Balakrishnaraja, R.S. Varma, S.S. Khan, *J. Water Process Eng.* **53**, 103657 (2023) https://doi.org/10.1016/j.jwpe.2023.103657.
15. S.A. Lachini, A. Eslami, M. Enhessari, *Int. J. Hydrogen Energy* **88**, 841 (2024) https://doi.org/10.1016/j.ijhydene.2024.09.172.
16. P. de Jesus Cubas, A.W. Semkiw, F.C. Monteiro, P. Los Weinert, J.F.H.L. Monteiro, S.T. Fujiwara, *J. Photochem. Photobiol. A: Chem.* **401**, 112797 (2020) https://doi.org/10.1016/j.jphotochem.2020.112797.
17. S. Mobini, F. Meshkani, M. Rezaei, *J. Environ. Chem. Eng.* **5** No 5, 4906 (2017) https://doi.org/10.1016/j.jece.2017.09.027.
18. M. Edrissi, S.A. Hosseini, M. Soleymani, *Micro Nano Lett.* **6** No 10, 836 (2011) https://doi.org/10.1049/mnl.2011.0430.
19. V. Novikov, G. Xanthopoulou, Y. Knysh, A.P. Amosov, *Ceram. Int.* **43** No 15, 11733 (2017) https://doi.org/10.1016/j.ceramint.2017.06.004.
20. E.T. Saka, K. Tekintas, *J. Molec. Struct.* **1215**, 128189 (2020) https://doi.org/10.1016/j.molstruc.2020.128189.
21. S. Balasurya, A.M. Elgorban, A.H. Bahkali, M.T. Yassin, R. Balakrishnaraja, R.S. Varma, S.S. Khan, *J. Water Process Eng.* **53**, 103657 (2023) https://doi.org/10.1016/j.jwpe.2023.103657.
22. T.C. Anusree, A.A. Vargeese, *J. Solid State Chem.* **315**, 123481 (2022) https://doi-org.www.sndl1.arn.dz/10.1016/j.jssc.2022.123481.
23. M.H. Habibi, F. Fakhri, *J. Therm. Anal. Calorim.* **115** No 2, 1329 (2014) https://doi.org/10.1007/s10973-013-3480-x.
24. S. Besra, K. Belakroum, S. Iaiche, D. Aouf, Y. Rahmani, H. Belkhalfa, A. Henni, *Solid State Sci.* **143**, 107282 (2023) https://doi.org/10.1016/j.solidstatesciences.2023.107282.
25. B.D. Cullity, R. Smoluchowski, *Phys. Today* **10** No 3, 50 (1957) https://doi.org/10.1063/1.3060306.
26. Y. Xu, X. Liu, X. Kan, S. Feng, W. Wang, C. Liu, Y. Li, *J. Supercond. Novel Magn.* **35** No 3, 753 (2022) https://doi.org/10.1007/s10948-021-06099-z.
27. P.S. Sathiskumar, C.R. Thomas, G. Madras, *Industr. Eng. Chem. Res.* **51** No 30, 10108 (2012) https://doi.org/10.1021/ie301435r.
28. P.M. Pimentel, M.F. Ginani, A.E. Martinelli, D.M.A. Melo, A.G. Pedrosa, M.A.F. Melo, *Mater. Sci. Forum* **498**, 663 (2005) https://doi.org/10.4028/www.scientific.net/MSF.498-499.663.
29. M.H. Habibi, F. Fakhri, *Synth. React. Inorg., Metal-Organ*
30. *., Nano-Metal Chem.* **46** No 6, 847 (2016) http://dx.doi.org/10.1080/15533174.2014.989591.
31. S. Heni, S. Hcini, M.L. Bouazizi, L. HajTaieb, A. Dhahri, H. ben Bacha, *RSC Adv.* **14** No 36, 26340 (2024) https://doi.10.1039/d4ra03342f.
32. E.B. Rubin, Y. Chen, R. Chen, *Sol. Energy Mater. Sol. C.* **195**, 81 (2019) https://doi.org/10.1016/j.solmat.2019.02.032.
33. P. Sankudevan, R.V. Sakthivel, A. Prakasam, A.M. Al-Enizi, M. Ubaidullah, B. Pandit, M. Sundararajan, *J. Cluster Sci.* **34** No 3, 1527 (2023) https://doi.org/10.1007/s10876-022-02328-0.
34. S. Landi Jr, I.R. Segundo, E. Freitas, M. Vasilevskiy, J. Carneiro, C.J. Tavares, *Solid State Commun.* **341**, 114573 (2022) https://doi.org/10.1016/j.ssc.2021.114573.
35. Y. Youn, J. Miller, K. Nwe, K.J. Hwang, C. Choi, Y. Kim, S. Jin, *ACS Appl. Energy Mater.* **2** No 1, 882 (2019) https://doi.10.1016/j.solmat.2019.02.032.
36. J. Hammouche, K. Daoudi, S. Columbus, R. Ziad, K. Ramachandran, M. Gaidi, *Inorg. Chem. Commun.* **131**, 108763 (2021) https://doi.org/10.1016/j.inoche.2021.108763.
37. A. Hernández-Gordillo, A.G. Romero, F. Tzompantzi, R. Gómez, *Appl. Catal. B: Environ.* **144**, 507 (2014) https://doi.org/10.1016/j.apcatb.2013.07.030.
38. J.A. Herrera-Melián, A.J. Martín-Rodríguez, A. Ortega-Méndez, J. Araña, J.M. Doña-Rodríguez, J. Pérez-Peña, *J. Environ. Manag.* **105**, 53 (2012) https://doi.org/10.1016/j.jenvman.2012.03.044.
39. S. Kumar, A. Tahira, A.L. Bhatti, M.A. Bhatti, Z.A. Ujjan, U. Aftab, Z.H. Ibupoto, *J. Energy Storage* **77**, 109994 (2024) https://doi.org/10.1016/j.est.2023.109994.

Синтез і характеристика наноструктур шпінелі $CuCr_{1.4}Co_{0.6}O_4$: вплив легування кобальтом на оптичні та фотокаталітичні властивості

Soumaia Khaldi[1], Abdelfattah Allaoui[1], Louiza Zenkhri[1], Safa Besra[2], Ece T. Saka[3], Cagla Akkol[3]

[1] *Laboratory for Valorization and Promotion of Saharian Ressources (VPRS), Chemistry Department, Kasdi Merbah University, UKMO, 30000 Ouargla, Algeria*

[2] *Laboratory of New and Renewable Energies Development in Arid and Saharan Zones, University Kasdi Merbah, 30000 Ouargla, Algeria*

[3] *Inorganic Research Laboratories, Chemistry Department, Karadeniz Technical University, KTU, 61080, Trabzon, Turkiye*

У цій роботі оксиди шпінелі на основі міді з загальною формулою $CuCr_{2-x}Co_xO_4$ ($x = 0$ та 0.6) були синтезовані методом простої горіння з метою дослідження впливу включення кобальту на їхні структурні, морфологічні, оптичні та фотокаталітичні властивості. Зразки були охарактеризовані за допомогою рентгенівської дифракції (XRD), сканувальної електронної мікроскопії з енергодисперсійною спектроскопією (SEM–EDS) та дифузійної відбивної спектроскопії у видимому та ультрафіолетовому діапазонах (UV–DRS). Результати XRD підтвердили формування добре кристалізованої однофазної шпінелі для обох зразків – $CuCr_2O_4$ та $CuCr_{1.4}Co_{0.6}O_4$ – з нанорозмірними кристалітами, що свідчить про збереження шпінелевої структури після заміщення кобальтом. Зображення SEM показали агломеровані нанорозмірні зерна майже сферичної форми, а EDS підтвердив однорідний розподіл Cu, Cr, O та Co. Аналіз UV–DRS продемонстрував зменшення ширини оптичної забороненої зони від 2.81 еВ ($CuCr_2O_4$) до 2.65 еВ ($CuCr_{1.4}Co_{0.6}O_4$), що вказує на покращене поглинання світла. Фотокаталітичні властивості зразків були оцінені під УФ-опроміненням щодо деградації метиленового синього (MB) та 4-нітрофенолу (4-NP). Допований зразок $CuCr_{1.4}Co_{0.6}O_4$ продемонстрував значно вищу фотокаталітичну активність, досягаючи повної деградації MB та 72.9 % перетворення 4-NP протягом 15 хв, значно перевершуючи недопований $CuCr_2O_4$. Це покращення пояснюється підвищеною ефективністю розділення зарядів, зменшенням енергії забороненої зони та меншим розміром кристалітів унаслідок включення кобальту.

Ключові слова: Наноструктури шпінелі, Метод горіння, Оптичні властивості, Фотокаталіз, 4-нітрофенол.